12-2022

A Theoretical Trade-Off Between Wave Drag and Sonic Boom Loudness Due to Equivalent Area Changes on a Supersonic Body

Nolan L. Dixon
Utah State University

A THEORETICAL TRADE-OFF BETWEEN WAVE DRAG AND SONIC BOOM LOUDNESS DUE TO EQUIVALENT AREA CHANGES ON A SUPERSONIC BODY

by

Nolan L. Dixon

A thesis submitted in partial fulfillment
of the requirements for the degree

of

MASTER OF SCIENCE

in

Aerospace Engineering

Approved:

Douglas F. Hunsaker, Ph.D. Major Professor	Stephen A. Whitmore, Ph.D. Committee Member
Zhongquan Zheng, Ph.D. Committee Member	D. Richard Cutler, Ph.D. Vice Provost of Graduate Studies

UTAH STATE UNIVERSITY
Logan, Utah

2022

ABSTRACT

A Theoretical Trade-Off Between Wave Drag and Sonic Boom Loudness Due to Equivalent Area Changes on a Supersonic Body

by

Nolan L. Dixon, Master of Science

Utah State University, 2022

Major Professor: Douglas F. Hunsaker, Ph.D.
Department: Mechanical and Aerospace Engineering

The theoretical trade-off between wave drag and sonic boom loudness is not well understood for a morphing supersonic geometry. The Sears-Haack body is an axisymmetric geometry that minimizes wave drag for a given length and volume. The purpose of the present work is to obtain an axisymmetric geometry that minimizes sonic boom loudness as perceived from the ground for a given length and volume. Such a geometry can be defined through an equivalent area representation using a Fourier sine series. By using the equivalent area approach, the perceived loudness and wave drag can be studied simultaneously to compare solutions. In this work, a tool was developed that accepts a number of Fourier coefficients and produces the equivalent area distribution, ground pressure signature, perceived loudness, and wave drag for that set of Fourier coefficients. An optimization routine was used to search for the coefficients that produce the minimum noise. The candidates are compared against the Sears-Haack's equivalent area, ground pressure signature, perceived noise, and wave drag. These methods were used to obtain a Pareto front of solutions to better understand the theoretical trade-off between wave drag and perceived noise on the ground.

(61 pages)

PUBLIC ABSTRACT

A Theoretical Trade-Off Between Wave Drag and Sonic Boom Loudness Due to Equivalent Area Changes on a Supersonic Body

Nolan L. Dixon

The NASA University Leadership Initiative (ULI) titled "Adaptive Aerostructures for Revolutionary Civil Supersonic Transportation" consists of a team of university and industry partners studying the feasibility of reducing the perceived loudness of the sonic boom by introducing an adaptive geometry at localized regions of an aircraft's outer-mold line. The Utah State University AeroLab is a member of this ULI team and has produced low-fidelity tools to predict the aerodynamic and boom loudness effects from localized changes to the geometry.

Such changes to the geometry affect both the sonic boom loudness and wave drag; however, the precise relationship between boom loudness and wave drag is not well understood for a morphing supersonic geometry. The current work utilizes an equivalent area approach and expresses this equivalent area using a Fourier sine series. An optimization routine was used to search for the Fourier coefficients that produce a minimum perceived level of decibels of the sonic boom for an optimized equivalent area distribution. The results for each candidate are compared against the Sears-Haack's equivalent area, ground pressure signature, perceived noise, and wave drag. These tools were used to obtain a Pareto front of solutions to better understand the theoretical trade-off between wave drag and perceived noise on the ground as equivalent area changes on a supersonic geometry.

Dedicated to my parents.

ACKNOWLEDGMENTS

I want to express my gratitude for my advisor, Dr. Hunsaker, for giving me the opportunity to work and learn from him over the past two years. I greatly value Dr. Hunsaker's approach to the field of aerodynamics and the fundamental theories that create the foundation for this scientific field. I am grateful for his insight, attitude, and dedication to every aspect of his work. I am continually inspired by the support Dr. Hunsaker shows for each of his students, and I sincerely appreciate his commitment each individual student. His direction has been invaluable to this work and to my individual successes along the way.

I want to thank my family, friends, grandparents, and colleagues who have helped me each day throughout my time as a student. I would also like to thank my colleague, Troy Abraham, for his advice and guidance over the past two years. His ideas and insight have been irreplaceable to me as I completed this work.

This work is supported by the NASA *University Leadership Initiative* (ULI) program under federal award number NNX17AJ96A, titled "Adaptive Aerostructures for Revolutionary Civil Supersonic Transportation."

Nolan L. Dixon

CONTENTS

LIST OF TABLES

LIST OF FIGURES

NOMENCLATURE

$AXIE$	Axisymmetric body
OML	Outer mold line
$PLdB$	Perceived level of decibels on the ground from a sonic boom
ULI	University Leadership Initiative
A_E	Equivalent area of a supersonic body
A_L	Component of cross-sectional area due to lift
A_V	Component of cross-sectional area due to volume
A''	Second derivative of area
D_w	Wave drag
δp	Change in pressure
l	Length of the supersonic body
M	Mach number
n	Iteration number through the Fourier sine series
p_0	Undisturbed ambient pressure
r	Radius of axisymmetric body
S	Calculated area of a supersonic body
U_∞	Free stream velocity
V	Volume of the supersonic body
W	Weighted result between the multi-objective optimization function
x	Axial distance along the supersonic body
β	Prandtl-Glauert factor, $= \sqrt{M^2 - 1}$
γ_{sh}	Ratio of specific heats, $= 1.4$
Γ	Multi-objective optimization weighting variable
ϕ	Azimuth angle
θ	Glauert variable to re-dimensionalize length along the body
ζ	Normal projection of a cut along a plane aligned with the Mach angle

CHAPTER 1

INTRODUCTION AND LITERATURE REVIEW

1.1 The Sonic Boom, Wave Drag, and Motivation for Current Work

The implications of generating sonic booms has been an area of research for aerospace and aviation ever since mankind broke the sound barrier in 1947 [2]. Today, flights at supersonic speed are commonly achieved by military aircraft; however, the U.S. and other countries have prohibited commercial aircraft from flying at supersonic speeds over civilized airspace due to concerns with sonic boom loudness [3]. While civil supersonic transportation was made available with the Concorde, any supersonic cruising was constrained to oceanic routes [4]. Interest has increased recently in a revival of supersonic civilian transport, but the restrictions due to loudness are still in effect and have given rise to investigations into "quiet" supersonic travel [5].

The flight path restrictions on supersonic flight is largely due to the fact that the sharp changes in pressure that cause a sonic boom have caused structural damage to buildings, and produce a sound that is perceived by humans to be within the range of annoying to painful [6]. If the sonic boom's perceived level in decibels (PLdB) is reduced, civil supersonic flight could be permitted over continental routes. A current area of research among the supersonic community includes altering the outer mold line (OML) of an aircraft in specific regions to change the aircraft's geometry during flight. These geometric changes attempt to influence the shock waves emanating from the aircraft and thereby reduce the PLdB on the ground as a result [7, 8].

Since high-efficiency air travel is becoming more and more important in the public eye, sonic boom loudness research must necessarily be coupled with understanding its effects on wave drag. Wave drag is a form of aerodynamic drag resulting from the changes in pressure induced by shock [9]. This form of drag is only present in supersonic and transonic flow, yet

it heavily influences the top speed and overall efficiency of aircraft that cruise in these flow regimes. Wave drag is directly related to the total cross sectional area of an aircraft and its spatial derivative along the length of the aircraft [10]. Any change to the OML geometry will likely produce a noticeable change in area and pressure distribution on the aircraft, affecting both PLdB and wave drag [11].Herein lies a trade-off that must be considered when changing the OML geometry of a supersonic body. This work seeks to understand this trade-off by studying how changes in area simultaneously affect sonic boom loudness and wave drag.

1.2 The NASA University Leadership Initiative - Adaptive Aerostructures for Revolutionary Civil Supersonic Transportation

The current work is part of a collaboration with a five-year NASA University Leadership Initiative (ULI) titled "Adaptive Aerostructures for Revolutionary Civil Supersonic Transportation". The ULI consists of a team of universities and industry partners studying the feasibility of reducing the perceived loudness of the sonic boom by introducing an adaptive geometry at localized regions of an aircraft's OML.

Utah State University has been a part of this ULI for five years and was tasked with developing low-fidelity aerodynamic and sonic boom prediction tools to study the effect of geometric changes on PLdB. The early analysis in this effort focused on a "low-boom" supersonic aircraft concept developed by NASA [12–14]. In the program's first year, Giblette used a panel-method code developed by Boeing, titled PANAIR, in an effort to predict aerodynamic performance and generate a near-field pressure signatures [15]. Giblette noticed limitations to the number of panels PANAIR could use and saw violations of a number of linear supersonic assumptions when using more complex geometries. This resulted in large, non-physical shock patterns in the near-field pressure signature [16]. As an extension of Giblette's work, Carpenter et al. showed that regions of the low-boom concept aircraft produced widely-varying near-field pressure signatures even when analyzed using higher-fidelity CFD methods [17]. Bolander attempted to leverage the benefits of the low-fidelity tool by splicing low-fidelity near-field signatures with the high-fidelity results from Carpenter et al.

to create a single solution without the uncharacteristic shock issue [18].

Abraham used PANAIR early on in his study of boom mitigation but changed to using an equivalent area approach to bypass the limitations mentioned previously and to connect the high and low-fidelity methods being used in the ULI [1]. Other studies from the ULI transitioned to using an equivalent area approach and showed that altering the rate of change in equivalent area can influence the pressure signature towards a more desirable outcome for reducing PLdB [19, 20]. Additionally, this equivalent area approach allows the equivalent area to be used directly by the NASA atmospheric propagation tool, sBOOM, instead of providing the tool a near-field pressure signature [21]. Abraham's work focused on changing the equivalent area input and observing the influence on the resulting PLdB. Furthermore, Abraham studied which axial locations and magnitudes of the equivalent area changes would have the greatest affect in minimizing PLdB on the NASA 25D aircraft. Abraham has also conducted a study comparing wave drag prediction methods using axisymmetric bodies, which is relevant to the scope of this work [22].

1.3 Review of Drag in Supersonic Flow

There are three sources of drag in supersonic flight, namely: viscous drag, vortex drag, and wave drag. Viscous drag is directly related to the viscosity of the fluid surrounding the body and is affected by temperature and air density [23].

Vortex drag is due to the direction of flow above and below the wings. As air moves over a wing, the air on the lower surface of the wing is at a higher pressure than the the air on the upper surface of the wing. Eventually, the air on both surfaces reaches the wing tip and attempts to return to equilibrium. This creates a vortex on the end of each wing circling from the lower surface to the upper surface. The vorticity induces a change in angle of attack across the wing, which results in the lift force being rotated into the direction of the free-stream. This causes a drag component and is why vortex drag is sometimes referred to as induced drag [24].

Wave drag is unique to supersonic and transonic flow and is the result of pressure waves that emanate away from the vehicle. Much like how a boat traveling at high speeds creates a

wake across water, a supersonic aircraft creates a wake of compressed air. This compression results in pressure waves that push back against the aircraft and cause drag [23].

1.3.1 Shock Waves and Pressure Signatures

After the aircraft passes through the local flow region, the air pressure suddenly shocks to a new value, and the flow properties change dramatically [25]. This sudden change in air pressure within a short time interval (in milliseconds) is the primary source of the audible component of the sonic boom. The dramatic and nearly instantaneous change in flow properties over a small distance along the aircraft is the primary source of a shock wave.

These pressure changes are often studied as changes in pressure over time and are referred to as pressure signatures. Pressure signatures can be evaluated at any point away from the aircraft but are given specific names depending on how far the signature has propagated. The change in pressure closest to the body is known as a near-field signature. A change in pressure at least five body lengths away from the aircraft is known as a far-field signature, and the change in pressure at ground level is known as the ground-pressure signature. Pressure signatures closer toward the aircraft generally consist of multiple shock waves and tend to have a jagged appearance.

As the pressure signature propagates through the atmosphere, the pressure waves coalesce [26] forming an abrupt over-pressure followed by an under-pressure. This abrupt change causes ground pressure signatures to follow a general "N-wave" pattern because the signature has lost most of its jagged appearance and looks like a capital 'N'.

1.4 Discussion of Equivalent Area

Multiple publications have described the equivalent area as a way to represent a supersonic body's area of effect on the surrounding air. This representation is based on the body's geometric and aerodynamic characteristics. These publications form the basis of the summary provided in this work [27–29].

The equivalent area of a given body has two major components. The first component is due to volume, and the second is due to lift [30]. The volume component is a product of geometric characteristics, and the lift component is a product of aerodynamic characteristics. The lift is included in the equivalent area representation because the the equivalent area considers the entirety of the fluid being disturbed. This representation considers not only the volume existing within the fluid, and the aerodynamic forces The expression for equivalent area is shown in the equation

$$A_E(x, \phi) = A_V(x, \phi) + A_L(x, \phi) \tag{1.1}$$

where x is an axial distance along the body of the aircraft, ϕ is the azimuth angle, and A_V and A_L are the cross-sectional areas for volume and lift sliced through the body at the appropriate Mach plane [31]. The areas at the Mach plane are used because the area and lift distributions must be taken normal to the direction the shock waves are propagating off the body [29, 32].

1.5 Von Karman and Sears-Haack Bodies

The von Karman and Sears-Haack bodies are slender axisymmetric geometries that minimize wave drag under specific conditions. The von Karman body minimizes drag for a finite base area, and the Sears-Haack body minimizes drag for a given length and volume [33]. Both bodies begin with a point at their leading edge and do not have lifting surfaces. For the purposes of the present work, they are assumed to be at zero degrees angle of attack and therefore produce zero lift. This assumption reduces Eq. (1.1) to only the volume component as a function x and ϕ [23]. Figure 1.1 shows the geometrical representation of a von Karman and Sears-Haack body.

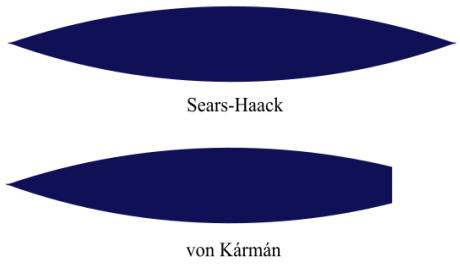

Fig. 1.1: Visual representation of the Sears-Haack body and the von Karman Ogive body.

The general distribution of azimuth angles relative to a supersonic body is shown in Figure 1.2.

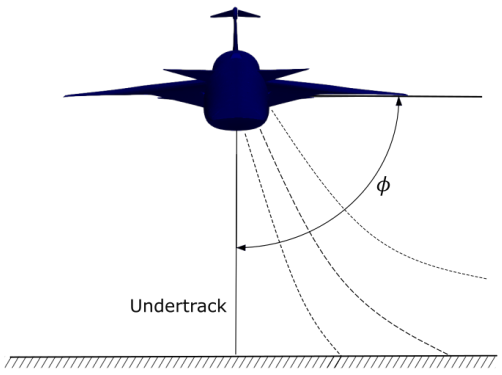

Fig. 1.2: Azimuth angle relative to a supersonic body [1].

The solution to Eq. (1.1) is specific to a single axial location at a given azimuth angle. A distribution of equivalent area can be generated as x sweeps through the full axial distance of the aircraft. At this point, the solution is only referencing a single azimuth angle on the aircraft, so the current description is limited to two dimensions. To get a complete picture of the equivalent area for the entire body, the same process can be repeated for multiple azimuth angles.

When studying the sonic boom, the primary region of interest is the under-track, so ϕ is directly beneath the supersonic body at $\phi = 0$. When studying wave drag, one must

consider all surfaces on the aircraft, so ϕ is swept through a full 360 ° rotation. Each equivalent area distribution is for the entire axial distance at a given ϕ creating a body of revolution. This body of revolution has the same area and lift distribution as the original three-dimensional body.

1.6 Wave Drag, Equivalent Area, and The Sonic Boom's Relation to Pressure

The sonic boom and wave drag both stem from the pressure distribution on a body, so understanding their mathematical relationship leads to identifying key components in their equations. For example, the audible component of the sonic boom is due to a rapid increase in air pressure. Therefore, identifying terms that influence the overall change in pressure can give insight into understanding their relationship to the loudness of the sonic boom. The same method can be applied to wave drag. The surface pressure around the body can be integrated along its length to determine wave drag if no lift is produced. Therefore, by identifying terms that minimize the surface pressure, one is able to isolate specific terms and their contribution to wave drag. Both scenarios are mathematically related to the air pressure and its reaction to the supersonic body.

Plotkin presented the mathematical relationship for a change in pressure in his review of sonic boom theory [31] as

$$\delta p(x-\beta r, r) = p_0 \frac{\gamma_{sh} M^2 F(x-\beta r)}{(2\beta r)^{1/2}} \tag{1.2}$$

where

$$F(x-\beta r) \tag{1.3}$$

is the Whitham F function [27], given as

$$F(x) = \frac{1}{2\pi} \int_0^X \frac{A''(\zeta)}{(x-\zeta)^{1/2}} d\zeta \tag{1.4}$$

Note Eq. (1.4) has the second derivative of area with respect axial location in the numerator. This term indicates it is not the area itself that affects the disturbance in pressure, but it is the change in rate of area growth that is significant when determining the F-function and subsequent change in pressure for the supersonic body. The area occupied by a supersonic body is not as significant as the rate at which the area comes in contact with the surrounding fluid [29]. This means a supersonic body must decrease the change in rate of area growth to decrease the overall wave drag on the body.

In 1956, Whitcomb published a paper on an idea that became known as the "supersonic area rule". He discovered wave drag can be reduced by thinning the fuselage of the aircraft at the locations of the wings and slightly thickening the fuselage in areas other than the wings. This decreases the wave drag because it decreases the rate at which the equivalent area is changing at a region of large increase due to the addition of each wing. By reducing the area over the wings, the wings can keep the same geometric characteristics and only the fuselage has to be modified to decrease wave drag [10]. This disperses the rate of change in area throughout the axial distance of the aircraft. Figure 1.3 shows this modification at the location of the wings.

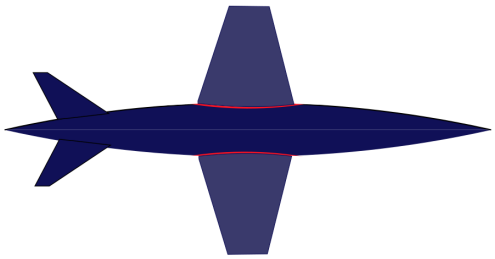

Fig. 1.3: Top-down view of the Whitcomb modification to the fuselage (shown in red) on an aerodynamic body.

1.6.1 Wave Drag, Equivalent Area, and The Sonic Boom's Relation to Mach

The Whitham F function shown in Eq. (1.4) also shares a relationship with the Mach number because the equivalent area is sliced by the Mach planes. This means the Mach

carries significance in both Eq. 1.2 and Eq. 1.4 [31]. For simple axisymmetric bodies, Lomax and Heaslet [34] showed that a good approximation for Mach-plane sliced area distributions can be achieved by slicing the area distributions at the plane perpendicular to the longitudinal axis. This work begins with the equivalent area distribution of the Sears-Haack body, so the same assumption made by Lomax and Heaslet can be made in this work. The Mach number will not change throughout the work and will be considered as part of the control variables to define the given flight conditions.

1.7 Wave Drag and Equivalent Area from Fourier Coefficients

In their work, *Aerodynamics of Wings and Bodies*, Ashley and Landahl outline a way to expresses the equivalent area distribution of an axisymmetric body using a Fourier sine series [23]. A summary of the process is described in this section.

The fundamental equation for the wave drag of a lineal source distribution can be written as

$$D_w = -\frac{p_\infty U_\infty^2}{4\pi} \int_0^l \int_0^l f'(x_1) f'(x_2) \ln |x_1 - x_2| dx_1 dx_2 \tag{1.5}$$

Assuming a slender body, the first derivative of area can be written as a function of x.

$$f(x) = S'(x) \tag{1.6}$$

where x is the axial distance along the body, and S is the equivalent area. Then using a change of variables to get from x to θ, the axial location along a body can be written as,

$$x = \frac{l}{2}(1 + \cos\theta) \tag{1.7}$$

where the nose represents $\theta = \pi$ and the base by $\theta = 0$. This is visualised using Figure 1.4.

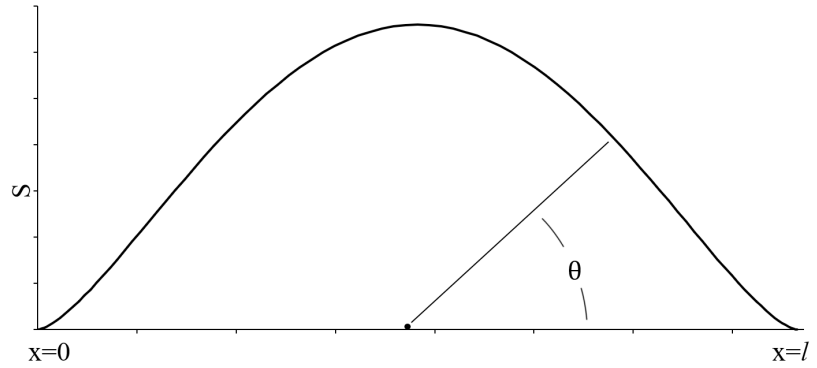

Fig. 1.4: Change of variables on an axisymmetric body between x and theta where $\theta = \pi$ represents the leading edge and $\theta = 0$ represents the trailing edge of the body.

Eq. (1.7) can be rearranged for θ where,

$$\theta = \arccos(\frac{2x}{l} - 1) \tag{1.8}$$

With this change of variables, Eq. (1.6) can be expressed as a Fourier sine series

$$S'(\theta) = f = l \sum_{n=1}^{\infty} A_n \sin(n\theta) \tag{1.9}$$

By solving the double integration in Eq. (1.5), the equation for wave drag can be simplified to

$$D_w = \frac{\pi p_\infty U_\infty^2 l^2}{8} \sum_{n=1}^{\infty} n A_n^2 \tag{1.10}$$

The area distribution can be written as a function of θ and a summation of the Fourier sine series

$$S(\theta) = \frac{l^2}{4} A_1 \left(\pi - \theta + \frac{sin(2\theta)}{2} \right) + \sum_{n=2}^{\infty} A_n \left[\frac{\sin(n+1)\theta}{n+1} - \frac{\sin(n-1)\theta}{n-1} \right] \tag{1.11}$$

An additional integration of area yields the total volume

$$V = \frac{\pi l^3}{8} (A_1 - \frac{1}{2} A_2) \tag{1.12}$$

where Eq. (1.12) is only dependent on the first and second Fourier coefficients, A_1 and A_2. This is significant because A_1 and A_2 are not free variables and the total volume will remain constant regardless of how many coefficients are chosen and at what magnitude they are chosen. Furthermore, this means each Fourier coefficient A_n represents a weight added to the Fourier sine series and are the only coefficients used to modify the equivalent area distribution. In other words, these coefficients determine the resulting change in equivalent area based off the Fourier sine series summation from Eq. (1.11). When working with the von Karman and Sears-Haack bodies, the first Fourier Coefficients equate to specific values, depending on the which body is being described.

For the von Karman scenario, A_1 is the only coefficient that contributes to the finite base area, as $\theta = 0$. By solving Eq. (1.11) for the first Fourier coefficient, A_1 is defined as

$$A_1 = \frac{4S(l)}{\pi l^2} \tag{1.13}$$

and any coefficient beyond A_1 is set to zero. This also reduces the equivalent area distribution in Eq. (1.11) to

$$S = \frac{S(l)}{\pi}\left(\pi - \theta + \frac{1}{2}\sin 2\theta\right) \tag{1.14}$$

By using Eq. (1.10), the generic equation for wave drag can be expressed as a function of the area distribution without additional coefficients, which is shown by the equation

$$D_w = \frac{2\rho_\infty U_\infty^2}{\pi}\frac{[S(l)]^2}{l^2} \tag{1.15}$$

Dividing Eq. (1.10) by the dynamic pressure and length gives the wave drag coefficient for the von Karman case, which is expressed through

$$C_{Dw} = \frac{4}{\pi}\frac{S(l)}{l^2} \tag{1.16}$$

For the Sears-Haack scenario, the Fourier Coefficient A_1 is zero due to the point at each end of the geometry, and the second Fourier Coefficient, A_2, is related to the geometry

volume and length according to

$$A_2 = -\frac{16V}{\pi l^3} \tag{1.17}$$

The area distribution for the Sears-Haack body is given as

$$S(\theta) = \frac{4V}{\pi l}\left(\sin\theta - \frac{1}{3}\sin 3\theta\right) \tag{1.18}$$

Using Eq. (1.11) and Eq. (1.15) with only A_1 and A_2 in the Fourier sine series gives the wave drag for the Sears-Haack body. This is expressed using

$$D_w = \frac{64V^2}{\pi l^4} p_\infty U_\infty^2 \tag{1.19}$$

Dividing by the dynamic pressure and length gives the wave drag coefficient, which is described by

$$C_{D_w} = \frac{24V}{l^3} \tag{1.20}$$

These relationships connect the Fourier coefficients of the Sears-Haack and von Karman bodies to their equivalent area representations and define the initial values for A_1 and A_2 depending on which body is being described. The initial values for A_1 and A_2 remain constant regardless of how many coefficients are added to the Fourier sine series. In subsequent sections, the coefficients including A_3 up to A_n will be used in a sample case to modify the equivalent area distributions and produce a new geometry to study. Furthermore, these equations outline the process to produce a wave drag estimate based on equivalent area described by the Fourier coefficients.

CHAPTER 2

COMPUTATIONAL METHODS AND TOOLS

2.1 Tool Integration and Sample Case Study

This chapter outlines the tool integration and methods used in studying the trade-off between wave drag and PLdB. In order to attain greater understanding of the design space in regards to any change in Fourier coefficients, an initial sample case was designed to sweep through a single Fourier coefficient, A_3, and note the effect on equivalent area distribution, ground pressure signature, and boom loudness. The sample case also served as a preliminary checkpoint to verify the tools were working properly and demonstrate the tool workflow.

For the purposes of the sample case, the equivalent area of the axisymmetric body is expressed using five Fourier coefficients, A_1 through A_5, using the equation

$$S(\theta) = \frac{l^2}{4} A_1 \left(\pi - \theta + \frac{\sin(2\theta)}{2} \right) + \sum_{n=2}^{\infty} A_n \left[\frac{\sin(n+1)\theta}{n+1} - \frac{\sin(n-1)\theta}{n-1} \right] \tag{2.1}$$

where $n = 5$. Equation 2.1 is the same equation presented in Chapter 1 but repeated here for convenience. Coefficients A_1 and A_2 are defined by the Sears-Haack Geometry mentioned in Chapter 1, and any coefficient beyond A_2 is considered a free variable since it is not fixed by the geometry.

2.1.1 Propagation Through sBOOM and PyLdB

The equivalent area distribution is generated using Eq. 2.1 and given to the NASA atmospheric propagation tool titled sBOOM. sBOOM requires an equivalent area distribution, the Mach number, the altitude, a reference body length, and the distance to start and stop propagating the signature. Each of these inputs are important to fully define the flight conditions. For example, the Mach number affects the shock waves emanating from

the geometry, the pressure intensity, and it quantifies the overall speed of the axisymmetric body. The altitude is significant because it defines the space in which the pressure is allowed to propagate, which affects many aspects of the boom as outlined in Chapter 1.

sBOOM uses the equivalent area distribution to generate a near-field pressure signature, propagates the pressure signature through a standard atmosphere, and returns the pressure signature perceived from the ground. That signature is given to an in-house tool called PyLdB. PyLdB is a python script that uses Stevens' perceived loudness method [35] to predict the PLdB observed at the ground for a given ground pressure signature. The PLdB value is generated using PyLdB, and the wave drag is calculated using Eq. (1.10). The PLdB, wave drag, equivalent area distribution, and ground pressure signature for the current set of Fourier coefficients are recorded, and A_3 is incremented to create a new set of Fourier coefficients. Coefficients A_4 and A_5 were not altered with each set of coefficients, as it was important to verify the tools were working properly and understand a single coefficient's affect on the equivalent area, boom loudness, and ground pressure signature. The process was repeated with the new A_3 coefficient until all increments of design variable sweeps were complete. If a negative equivalent area was detected, the code skipped the current execution and no results were recorded for that set of Fourier coefficients.

2.2 Sears-Haack Sample Case

A Sears-Haack body was chosen as the geometry for the sample case. A body length of 38.26 meters was chosen to match that of the NASA 25D experimental aircraft with a volume of 29.726 cubic meters. The Mach number was set to 1.6, and the altitude was initialized to 50,000 feet. sBOOM was initialized to begin propagating at five body-lengths away and to stop propagating once the signature reached the ground.

Coefficient $A_1 = 0$ and coefficient A_2 was defined using Eq. (1.17). The coefficient A_3 was initialized at -0.002, and an increment value for A_3 was set to 0.00025. The Fourier coefficients A_4 and A_5 were set equal to -0.002 and 0, respectively. The coefficient A_3 was incremented after each result, for a total of 18 solutions. The wave drag was calculated for each set of Fourier coefficients using Eq. (1.19) using the prescribed volume and length.

The PLdB was compared against the wave drag for each set of Fourier Coefficients, and the results are shown in Figure 2.1. To improve readability, only half of the results are shown.

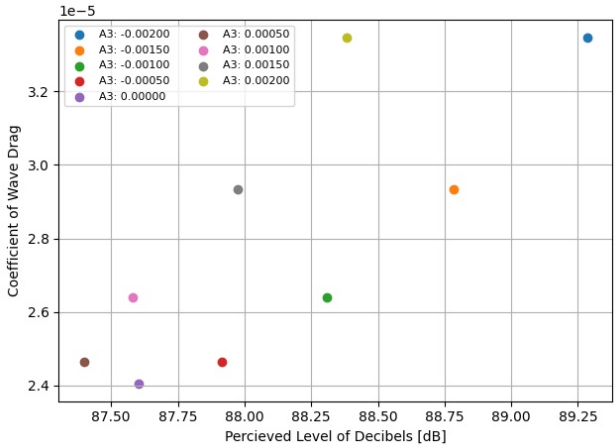

Fig. 2.1: Study showing the relationship between PLdB and wave drag as the Fourier coefficient A_3 is incremented through a range of values.

This study served as a means of verifying the tool integration and showed PLdB and wave drag share a relationship with a change in equivalent area. This study also showed that changing a single coefficient will reach an instance where the trend where PLdB is being minimized turns back on itself. This test case showed that altering a single coefficient would not be sufficient in reducing the PLdB, as the solutions eventually mirror themselves as the coefficient changes from positive to negative. Therefore, an optimizer would be used to adjust multiple coefficients and find equivalent area distributions that minimized the objective. These minimums can then be used to find Pareto fronts between the Sears-Haack solution and the solutions that minimize noise.

The equivalent area distributions for each set of Fourier coefficients were visualised in Figure 2.2. Note the figure only shows every other A_3 increment to improve readability, but the overarching trends remains.

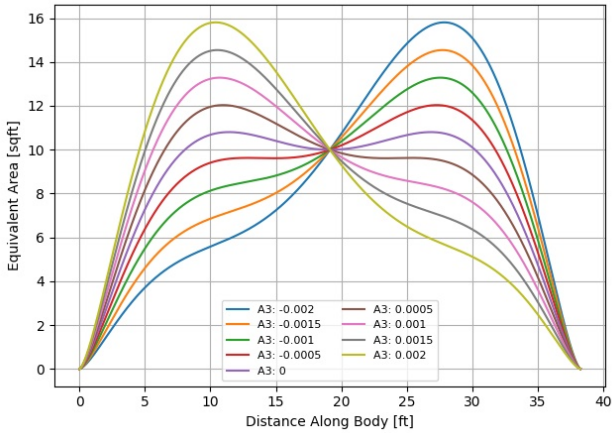

Fig. 2.2: Study showing the shifts equivalent area as A_3 is incremented from negative to positive.

A negative A_3 value shifted the area distribution aft, and a positive A_3 value shifted the area distribution forward. It is important to note that the case where A_3 was equal to zero was not the Sears-Haack case because A_4 was set to -0.002 for each set of Fourier coefficients used in this sample case. This study also showed that the equivalent area shifted systematically as the coefficient A_3 incremented through the allowed range.

The ground pressure signatures associated with the sets of Fourier coefficients are plotted at every other increment of A_3, and the results are shown in Figure 2.3.

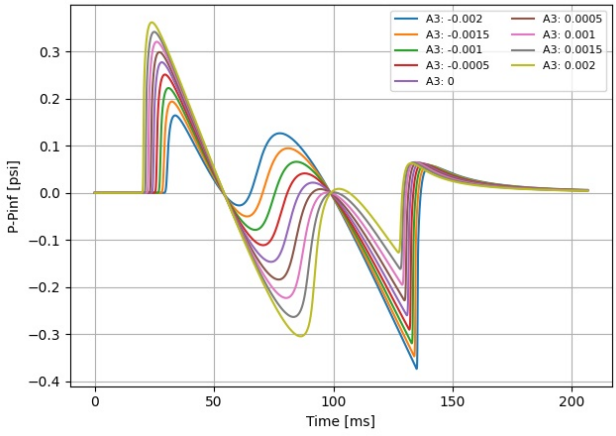

Fig. 2.3: Ground pressure signatures at periodic increment of A_3 with shaped characteristics.

The loudest signatures in the sample case were those with the largest over pressures and under pressures, as these signatures demonstrated the sharpest deviation from ambient pressure in the shortest time interval.

CHAPTER 3

OPTIMIZATION ROUTINES AND EXPOSURE TO THE DESIGN SPACE

3.1 Fourier Coefficients and the Equivalent Area

To get an initial exposure to the design space, a digital spreadsheet was created that accepted four Fourier coefficients and plotted the resulting equivalent area distribution. The coefficients A_1 and A_2 were defined in Chapter 1, and coefficients A_3 and A_4 were again designated as free variables. A slider was created that allowed A_3 and A_4 to be adjusted in small increments, and the resulting equivalent area was compared to the equivalent area of the Sears-Haack. Some Fourier coefficient combinations produced a negative equivalent area at some points along the body. An area distribution with any negative area values represents something non-physical. Therefore, the set of Fourier coefficients must produce an area distribution with all points being positive to produce valid results.

This spreadsheet also gave insight into each coefficient's effect on the equivalent area. The sheet was altered to accept A_5-A_10, and coefficients A_3-A_10 were initialized to zero. Each coefficient was tested individually by setting its value equal to ± 0.005 and observing the results. A positive A_3 created two peaks in the sine function and shifted the area forward, while the negative value of A_3 created two peaks of the same magnitude with the area shifted aft. A positive A_4 created a sine function with three peaks, and the negative A_4 value simply redistributed the area between the three peaks.

The coefficient A_5 produced a curve with four peaks, and A_6 produced and expression with five peaks. This pattern held true for A_7 through A_10. Increasing the magnitude of the coefficients exaggerated the expressions sinusoidal behavior, which resulted in more drastic amplitudes between peaks. These patterns remained the case for the rest of the design variables. Lastly, this tool provided an estimate for the orders of magnitude needed by the Fourier coefficients to produce reasonable results. A value of ± 0.005 frequently created sine

functions that contained negative values, so future tests required a smaller magnitude.

3.2 Defining Bounds for the Optimization Routine

Using the methods outlined by the sample case in Section 2.2, the Fourier coefficients A_3 and A_4 were swept from -0.003 to 0.002 at set increments while reporting PLdB and wave drag for each combination. The Mach number was set to 1.4, and the altitude was set to 50000 feet. The coefficients A_5-A_10 were not included in this study, as the goal was simply to find a suitable range of values to search for an optimum solution. Additional coefficients, such as A_5-A_10, will be included in the optimization routines, but were not included at this point.

The PLdB values were lowest when A_3 and A_4 were each between values of ± 0.001. Negative equivalent areas were produced for A_4 values of 0.001, excluding the case when A_3 equaled zero. The results of the study are shown by the tables in the Figure 3.1 below.

PLdB						
	A4					
A3	-0.003	-0.002	-0.001	0	0.001	0.002
-0.002	90.658	89.047	88.195	-	-	-
-0.0015	90.329	88.541	87.546	87.152	-	-
-0.001	90.006	88.058	86.867	86.275	-	-
-0.0005	89.831	87.678	86.205	85.338	-	-
0.0	89.83	87.37	85.626	84.348	87.314	-
0.0005	90.028	87.165	85.261	83.498	-	-
0.001	90.493	87.386	85.281	83.218	-	-
0.0015	91.241	87.78	85.569	83.702	-	-
0.002	92.01	88.17	86.081	-	-	-

(a) PLdB

Wave Drag						
	A4					
A3	-0.003	-0.002	-0.001	0	0.001	0.002
-0.002	4.918	3.347	2.4	-	-	-
-0.0015	4.505	2.934	1.99	1.678	-	-
-0.001	4.211	2.64	1.69	1.383	-	-
-0.0005	4.034	2.463	1.521	1.207	-	-
0.0	3.975	2.404	1.462	1.148	1.462	-
0.0005	4.034	2.463	1.521	1.207	-	-
0.001	4.211	2.64	1.697	1.383	-	-
0.0015	4.505	2.93	1.992	1.678	-	-
0.002	4.918	3.347	2.4	-	-	-

(b) Wave Drag Coefficient $1e^{-}5$

Fig. 3.1: PLdB and wave drag produced from the initial sweep through A_3 and A_4.

As a result of this study, all free variables were bound between ± 0.001 for the future optimization routines, as A_3 and A_4 produced the lowest drag and PLdB values when they were within said range.

3.3 Visualization Through Two-Dimensional Slices of the Design Space

At this point, it was unclear if the design space contained smooth gradients between PLdB values or if it contained multiple local minima throughout the design space. There-

fore, the next step was to generate contour plots by setting A_5 and A_6 to zero while sweeping A_3 and A_4 through the bounds mentioned above. These results were used to create a contour plot of PLdB for combinations of A3 and A4. Some combinations of A_3 and A_4 generated a negative equivalent area, and these locations were denoted as white space around the contour lines to represent infeasible combinations of A_3 and A_4. The contour plot for A_3 and A_4 is shown in Figure 3.2.

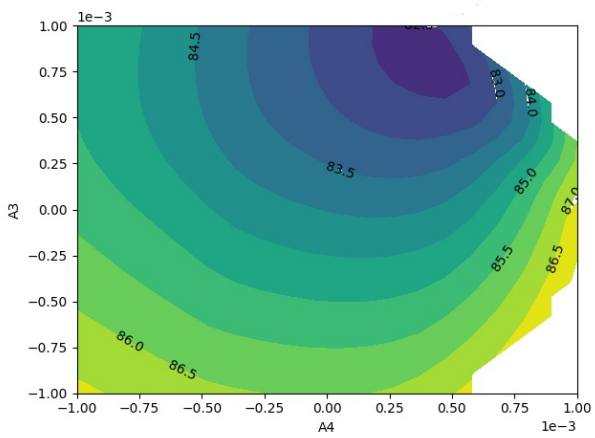

Fig. 3.2: Contour plot of PLdB for combinations of A_3 and A_4 holding A_5 and A_6 to 0.0.

The same process was repeated with A_3 and A_4 set to zero while sweeping A_5 and A_6 through the bounds set previously. The results are shown in Figure 3.3.

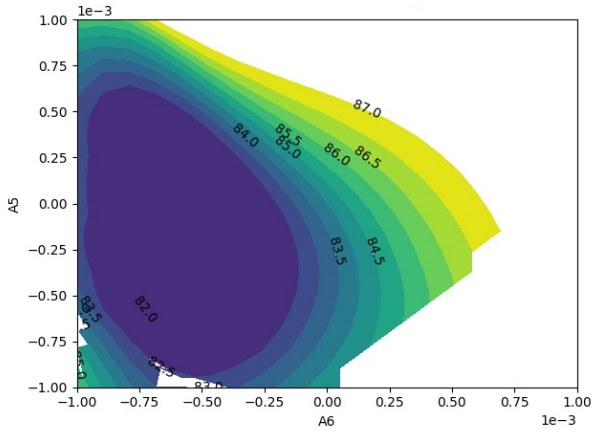

Fig. 3.3: Contour plot of PLdB for combinations A_5 and A_6 holding A_3 and A_4 to 0.0.

This study showed 2D slices through the design space appear somewhat well behaved when two of the coefficients are held constant. The contour plots are generally smooth, continuous, and appear to have one global minimum. This supported the researchers intent to test the design space using a gradient-based method.

3.4 Data Handling of Infeasible Solutions

Some combinations of Fourier coefficients produced a negative equivalent area, which is non-physical and indicates the entire equivalent area distribution cannot be used. In order to function properly, the optimization routines require a solution to the objective function at each instance. Therefore, even infeasible solutions were required to return a numerical value. With this in mind, the Python script was designed to return a value proportional to the PLdB value of the Sears-Haack plus a factor using the number of negative areas encountered in the current area distribution. This scaled the result of the constraint function to be proportional to the results of the Sears-Haack body and prevented the optimization routines from generating too steep of a cliff in any direction of the design space.

This positive area constraint was expressed as a non-linear inequality constraint so that the optimizer forced a positive result. The equivalent area was generated for each combination of Fourier coefficients at each value for θ along the axial distance of the geometry. The equivalent area distribution was tested, and the minimum equivalent area was returned by the constraint function. This scaled the constraint function by enforcing large penalties for a very negative area and a smaller penalty for an equivalent area that was only slightly negative.

3.5 Optimization Through a Genetic Algorithm

To test the design space further, SciPy's Differential Evolution algorithm was used to generate sets of Fourier coefficients to search for a minimum. Coefficients A_1 and A_2 remained the same as defined previously, and the remaining coefficients were designated as free variables for the optimizer to change.

The genetic algorithm was given a population size, a maximum iteration number, the number of generations to perform, and an initial guess. It found favorable results to minimize PLdB even when given the initial conditions of the Sears-Haack. However, the speed of the genetic algorithm was largely dependent on how close the initial guess was to an optimal solution. When given the Sears-Haack coefficients as the initial guess, the genetic algorithm took up to 13 hours to produce the coefficients that minimized PLdB.

Differential Evolution was profitable in that it wasn't at risk of becoming stuck at a local minimum, but it did take significantly more computing time than gradient-based optimization routines, especially as more coefficients were introduced as free variables.

Differential Evolution also used a polishing function that could be toggled via a Boolean input parameter. If the parameter was set to true, the polishing function would attempt a gradient-based method to polish the final results produced by the genetic algorithm. The polishing parameter was set to true for these results.

3.6 Optimization Through a Gradient Method

The next optimization routine used an in-house minimization tool created by the AeroLab at Utah State University called Optix. Optix is a gradient-based optimization tool and functions similarly to other minimization tools in Python's SciPy module. The SQP method was selected as the gradient-based routine because SQP can accept constraints, such as the positive equivalent area constraint required for this study. The SQP method was not guaranteed to enforce the constraint throughout the optimization process, but it was guaranteed to produce a result that satisfied the constraint.

The speed of the SQP method also showed a dependency on the initial guess. If the initial guess was close to a minimum, the SQP was able to find a set of Fourier coefficients for a quieter PLdB in about an hour or less. However, the SQP method sometimes produced results that were considered local minima. They were considered local minimum because other methods were able to find quieter solutions given the same initial guess.

Gradient-based methods are known for finding a solution quickly if the domain is well behaved, but they come with the drawback of sometimes getting stuck in a local minimum.

The fact that the SQP method reported some local minima led the researchers to believe that the domain is well behaved when taking a slice through the domain of two coefficients, but the design space becomes increasingly complex as more coefficients are introduced as free variables.

3.7 Optimization Through Nelder-Mead Method

The last optimization routine used the Nelder-Mead simplex method under the SciPy Minimization package. The Nelder-Mead method is a direct search method, in that it evaluates the objective function multiple times and systematically makes decisions to find the minimum solution.

When considering a two-dimensional design space, the Nelder-Mead method calls the objective function three times and forms a triangle between the three solutions. It evaluates which point is the largest among the three, and flips that solution over the line segment created by the other two points. It tests this flipped point to determine if it is smaller than its previous position. If it is, the process repeats. If it is not, the algorithm shrinks each leg of the triangle, and repeats the search. In higher dimensions n, the Nelder-Mead method uses $n+1$ function calls to optimize, and continues in the same manner described above.

The Nelder-Mead method does not require the derivative of the objective function to be known. It is able to handle bounds, but not constraints. Therefore, this method required the data to be handled as mentioned in Section 3.4.

3.8 Selection of an Optimization Method

When selecting an optimization method, it is important to define what aspects of the optimization are important for the study. For this work, it is important that the optimization routine not get stuck in any local minima and that it is reasonably time effective. The optimization routine needs to find solutions to approximately 100 cases, and if the optimizer takes 13 hours to find a solution for a single case, that could lead to an extensive amount of time even if the optimizer was constantly running.

The Nelder-Mead method was able to find solutions relatively quickly, and it was able to return solutions that were quieter than the gradient based method given the same initial guess, which marked it as a good initial candidate. Nelder-Mead is not guaranteed to find the global minimum. However, the Differential Evolution algorithm took 13 hours to find a solution to some test cases. Although Differential Evolution was an effective means to find valuable solutions, it's computationally expensive nature deterred the researchers from selecting it as the optimization routine for the rest of the studies in this work.

The SQP method was effective in finding solutions in a relatively short amount of time, but it did return solutions that were louder than the Nelder-Mead method for some test cases even when given the same initial guess. Therefore, the Nelder-Mead method was chosen as the optimization routine for the rest of the studies included in this work due to its computational speed and because it did not return any local minima during the test cases.

3.9 Multi-Objective Optimization

One of the main objectives of this work was to produce a Pareto front of solutions between the minimum drag solution and the solution that minimized PLdB. To achieve this result, a multi-objective optimization routine was implemented into the objective function within the optimizer that weighted the two solutions relative to each other.

A weighted parameter Γ was implemented into the following equation,

$$W = \Gamma * (D_w * 5 * 10^6) + (1.0 - \Gamma) * \text{PLdB} \tag{3.1}$$

where W was the weighted result, D_w was the coefficient of wave drag multiplied by a factor of $5 * 10^6$ to scale the wave drag to the same order of magnitude as the PLdB. This created a weighted average between the two solutions.

A Γ of 0.0 signified a solution solely weighted toward minimizing PLdB, and a Γ of 1.0 signified a solution solely weighted toward minimizing drag. The value of Γ could be set to any value between 0.0 and 1.0 to weight the solution by that percentage of wave drag and

use the remaining percentage to weight PLdB. For example, a Γ value of 0.2 will weight the objective function to optimize for 20% in the direction of wave drag and 80% in the direction of PLdB. With this multi-objective optimization routine in place, the optimizer was ready to run solutions that define the Pareto front between wave drag and PLdB.

CHAPTER 4

OPTIMIZATION RESULTS

4.1 Optimization with Nelder-Mead

The optimization routine was organized such that a number of design coefficients, N, could be specified. Coefficients A_1 and A_2 were the first two coefficients in each set, so the total number of coefficients in the Fourier series was always two greater than N. The routine was designed to minimize PLdB and wave drag by altering the design coefficients used in the Fourier sine series. The initial guess for each set of coefficients were defined, and Γ was set to a value between 0.0 and 1.0 depending on the desired weighting. The objective function was written to calculate the PLdB and wave drag result based on the current set of Fourier coefficients and use Eq. (3.1) to return a weighted result.

The Nelder-Mead algorithm was given the objective function, the initial guess for the design coefficients, and the bounds in which to operate. Once a solution was found, Nelder-Mead was called a second time with the Fourier coefficient results set as the initial guess for the next set of Fourier coefficients. This process repeated until two consecutive results matched to machine precision. At this point, a PLdB and wave drag solution were returned for the current weighting of Γ. This verification method helped ensure the optimizer would not stop prematurely and assist in making the optimizer more robust.

4.2 Pareto Front Generation

With the Nelder-Mead method in place, the optimization routine was used to generate the Pareto fronts by iterating on the design coefficients within the Fourier sine series. To generate a Pareto front, Γ was initialized at 0.0 and the initial guesses for A_3 through A_N were set to 0.0. After a solution was found for that specific Γ, the PLdB, wave drag, and the Fourier coefficients were recorded to a digital spreadsheet. The weighting parameter Γ was

incremented by +0.1, and the optimization was repeated using the previous solution as the initial guesses for A_3 through A_N. This process of using the previous Fourier coefficients as the initial guess for the next data point within the Pareto front assisted in connecting the solutions to each other across the design space and ensured the optimizer started in the same valley within the design space.

The optimization routine repeated this process from $\Gamma = 0.0$ to $\Gamma = 1.0$ to generate the data points for a single Pareto front. A CSV file was produced that listed the optimized Fourier coefficients with their respective PLdB and wave drag values. The PLdB and wave drag values were plotted on a digital spreadsheet to visualise the Pareto front for the number of design variables.

To generate subsequent Pareto fronts, the coefficients describing the minimum noise solution were used as the initial guess for the next Pareto front, and any additional design coefficients were initialized to 0.0. This process was repeated using 2 design coefficients to 18 design coefficients by adding two design coefficients to Eq. 1.11 with each new Pareto front. The Sears-Haack solution was marked and served as a reference for the minimum wave drag solution in each Pareto front. These Pareto fronts are shown in Figure 4.1.

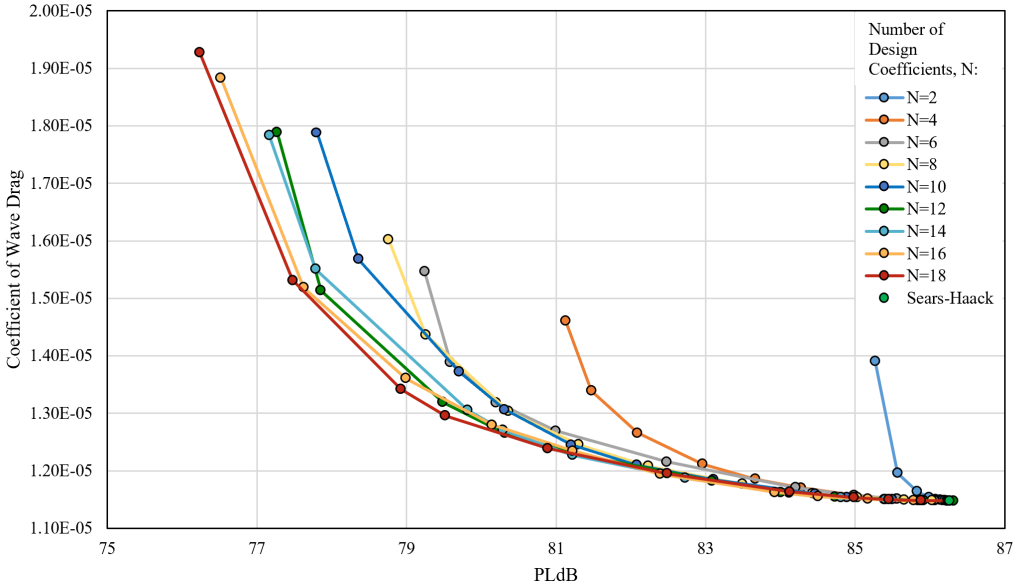

Fig. 4.1: Pareto front of wave drag to PLdB for a Mach of 1.6 using a number of design coefficients, N, compared to the Sears-Haack solution.

4.3 Discussion of Trade-Off Between PLdB and Wave Drag

Figure 4.1 shows that a trade-off exists between PLdB and wave drag as equivalent area changes on a supersonic body. The solution that minimizes noise is the solution that generates the most wave drag, and the solution that minimizes wave drag is the solution that generates the loudest boom. By looking at the curve when N=18, one can see a range of solutions that minimize these two objectives for different weighted solutions. Each solution set returned to that of the Sears-Haack as Γ approached 1.0. As the number of Fourier coefficients was increased, the minimum noise solution was able to produce a quieter result.

The minimum noise solution using 18 design variables produced a wave drag coefficient of 1.93E-05 with a PLdB value of 76.235 decibels, and the Sears-Haack solution produced a wave drag coefficient of 1.15E-05 and a PLdB value of 86.241 decibels. Based on these results, the PLdB value from an axisymmetric body could be reduced by approximately 10.03 decibels if it accepted a 67.96% increase to the coefficient of wave drag relative to the Sears-Haack solution when using 18 design variables.

The Pareto front when N=18 demonstrates the PLdB can be reduced significantly with only a marginal increase to wave drag with an appropriate weighting of Γ. This region is project dependent as it varies with the number of design coefficients N as well as Mach and other flight conditions, but in this work, the PLdB dropped from 86.265 dB to 79.518 dB with the wave drag increasing from 1.15E-05 to 1.30E-05. This translates to a 6.721 decrease in decibels for a 12.88% increase to wave drag.

The Pareto fronts in Figure 4.1 help visualise the minimum solutions for the two objectives across the design space. The information gained from these Pareto fronts connects two areas of research important to supersonic studies. This suggests a similar trade-off exists for all supersonic bodies that can alter their equivalent area distribution. Theoretically, these supersonic bodies could alter their equivalent area distribution in such a way to select a desired minimum noise and wave drag solution that lies along their respective Pareto front.

4.4 Convergence of Solutions

It is important to note that adding more design coefficients allowed for a greater spread in results. The attainable solutions when N=2 were not nearly as widespread as the solutions attained when N=18. This is because an equivalent area distribution created from two free variables is not as flexible as the curves with more free variables. In this case, the optimizer had less coefficients to adjust and lacked the ability to manipulate the equivalent area distribution due to the number of frequencies built into Eq. (1.11). This idea becomes apparent when considering the jump in solutions when N=2 to when N=4. The additional design variables allowed the optimization routine to manipulate the equivalent area distribution to where the PLdB and wave drag solutions could be minimized further. However, there comes a point where additional design coefficients become less significant with each additional design coefficient. The solutions generated in this work are shown in Figure 4.2

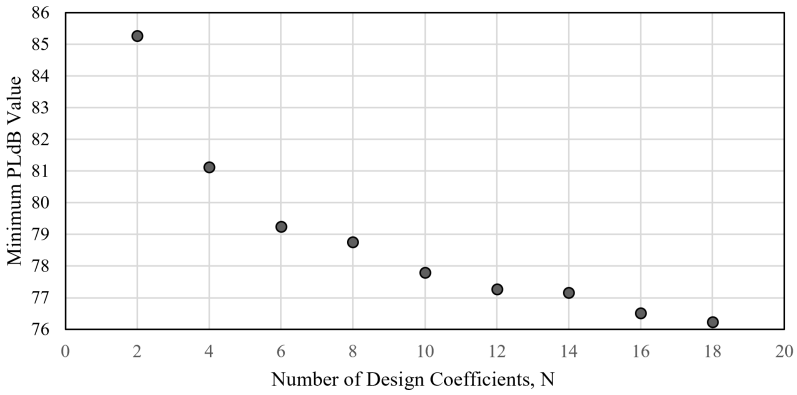

Fig. 4.2: Convergence of minimum PLdB values using N design coefficients.

The Pareto front describing the absolute achievable minima within the design space occurs when the optimization routine uses an infinite number of Fourier coefficients. However, testing such a routine with the method outlined in this work is not possible. The objective then transitions into testing a number of design coefficients where solutions begin to converge and to determine when adding additional coefficients begins to produce diminishing returns. The general trend in Figure 4.2 showed an increase to the number of design

coefficients produced a decreasingly significant change in the minimum PLdB.

The minimum solution using 10 design coefficients decreased more than what was expected based on the previous step, but it is important to note the significance of additional frequencies being added to the equivalent area representation. Each design coefficient being added to the expression adds an additional frequency to the system overall, and the human ear can be more sensitive to some frequencies than to others. This could give reason to why some frequencies are more sensitive to ears than others. The step change in minimum PLdB from N=8 to N=10 is much less than the jumps in PLdB from N=2 and N=4.

Based on the information in Figure 4.2, the solutions show the beginning of convergence but have not yet converged on a solution. Future work could include testing even more design variables to study the rate of convergence, but such a study is not done in this work. The researchers used 18 Fourier coefficients to describe the equivalent area of the NASA 25D with respect to volume, so the optimization process stopped after using 18 design coefficients. Adding additional coefficients would increase computing power and require additional time, but more design coefficients could be added beyond 18 to study the behavior of the system and could give insight into harmonic behavior in connection with the frequencies added into the system.

Figure 4.3 presents the absolute value of each coefficient, A3 to A20, along the Pareto front when N=18. From the figure, it can be seen that the coefficient A10 does not carry as much influence in the solutions compared to other coefficients. Further work could be done to investigate the frequencies introduced through each coefficient and understand the behavior of higher coefficients. The coefficients show a slight downward trend in order of magnitude when comparing the data set as a whole.

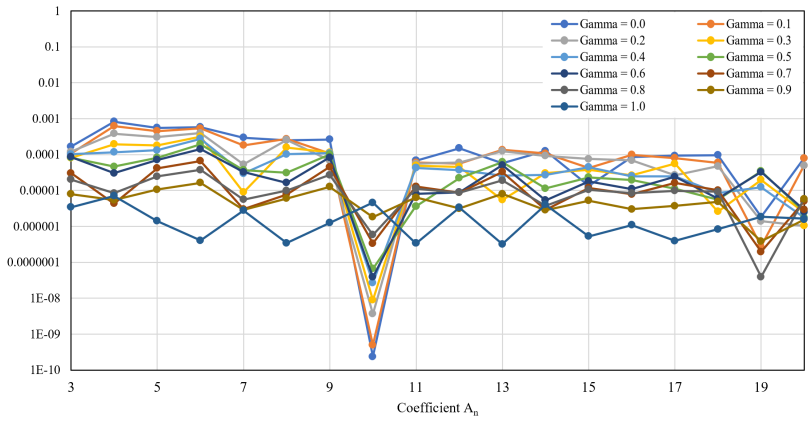

Fig. 4.3: Fourier coefficient values from A3 to A20 over different weighting distributions from minimum wave noise to minimum wave drag plotted on a log scale.

4.5 Limitations

As outlined in Chapter 1, the results in this work are created using only the volume component of the equivalent area representation. Further work would include adding the lift component to describe the equivalent area distributions used throughout this process.

The Sears-Haack axisymmetric body is assumed to be at zero degrees angle of attack for all cases in this study and does not have lifting surfaces. Therefore, the Sears-Haack body does not produce lift. The NASA 25D is an aircraft with lifting surfaces, and the equivalent area of the NASA 25D does have a lift component even when at zero angle of attack. However, the NASA 25D equivalent area distributions used in this work are strictly the volume component of equivalent area for the 25D as obtained through OpenVSP [36,37]. This difference between the bodies could give reason to why the equivalent area distribution for the NASA 25D is shifted further aft compared to the equivalent area distributions produced from the optimization routine.

Adding the lift component to the equivalent area would help to create a more complete picture of the relationship between wave drag and PLdB, but such a solution is beyond the scope of this work and is left for future researchers to implement. The lift component adds complexity to the Fourier sine series, as it would require the sine series to generate a less harmonic shape such that the equivalent area distribution would not return to zero at the

trailing edge. Rather, the area distribution would end at a finite value to signify lift. In this case, the von-Karman axisymmetric body may be more appropriate of a comparison in a similar study as that done here.

4.6 Comparison of Equivalent Areas as a Function of Coefficients

This section presents the equivalent area distributions for different numbers of design variables as Γ shifted from 0.0 to 1.0. A Γ value of 0.0 represented an objective weighted solely toward minimizing PLdB, and a Γ of 1.0 represents an objective weighted solely toward minimizing wave drag. Figure 4.4 shows the shifts in equivalent area distribution for two design variables for different weighting parameters.

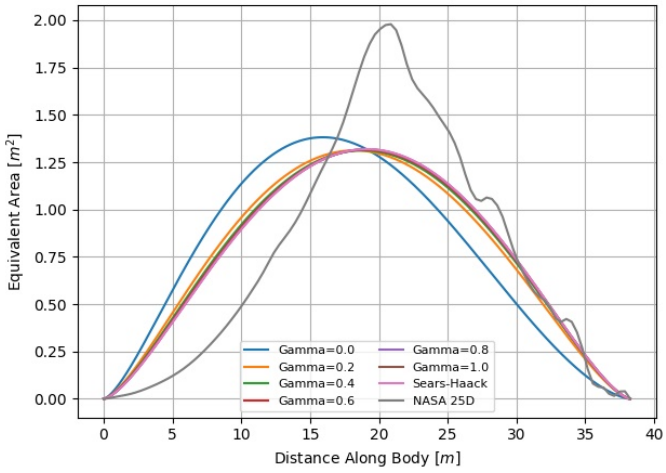

Fig. 4.4: Shifts in equivalent area distribution as the objective function shifts from minimizing boom to minimizing drag when using two design coefficients.

Here, the spread in results is minimal due to only having two design coefficients to optimize, so the solution that minimizes noise is not significantly different from that which minimizes drag. The minimum noise solution is similar in shape to the Sears-Haack, except that it is shifted slightly forward along the body. With only two design coefficients, the Fourier sine series is limited in its flexibility.

When four design coefficients are used, the spread in equivalent area distributions becomes more noticeable, and the minimum noise solution begins shifting toward the equivalent area distribution of the NASA 25D. The minimum noise solution is narrower than the Sears-Haack solution. This result is shown in Figure 4.5.

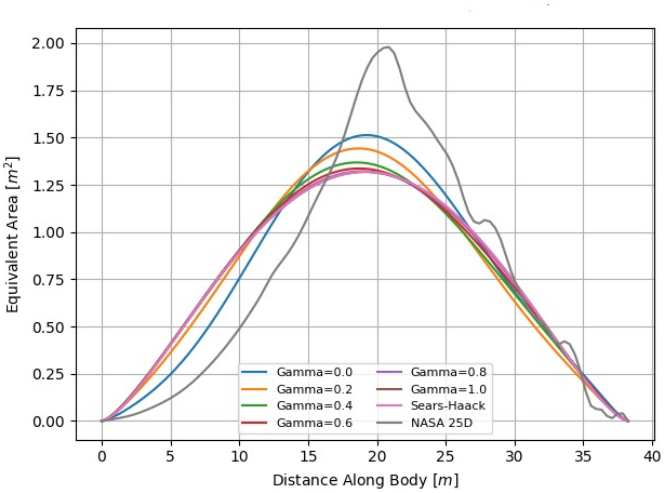

Fig. 4.5: Equivalent area distributions as the objective function shifts from minimizing boom to minimizing drag when using four design coefficients.

With six design coefficients, the minimum noise solution shifts forward along the axial distance, which is in the same direction as the minimum noise solution that used two design coefficients. The minimum noise solution still favors an increasingly narrower shape as more coefficients are added. This trend is shown in Figure 4.6.

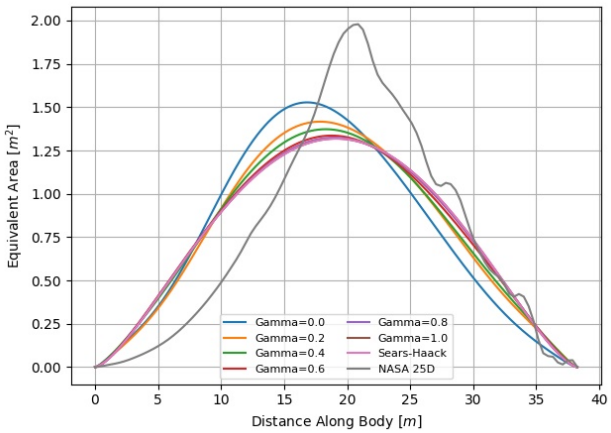

Fig. 4.6: Equivalent area distributions as the objective function shifts from minimizing boom to minimizing drag when using six design coefficients.

The equivalent area of the minimum noise solution using 8 design coefficients continues to drop below that of the Sears-Haack at the leading and trailing edge by redistributing this area towards the center of the body. This creates a higher peak with each shift in Γ towards minimizing PLdB. The height of the peak has increased with each step towards minimum noise. This indicates the minimum noise solution will become increasingly taller as more coefficients are added as the solutions converge.

A similar pattern is shown by the equivalent area distribution of the NASA 25D aircraft. The NASA 25D's distribution has less equivalent area along the nose and droops significantly below that of the Sears-Haack. It also has a high peak value near the center location along the body. These relationships are shown in Figure 4.7.

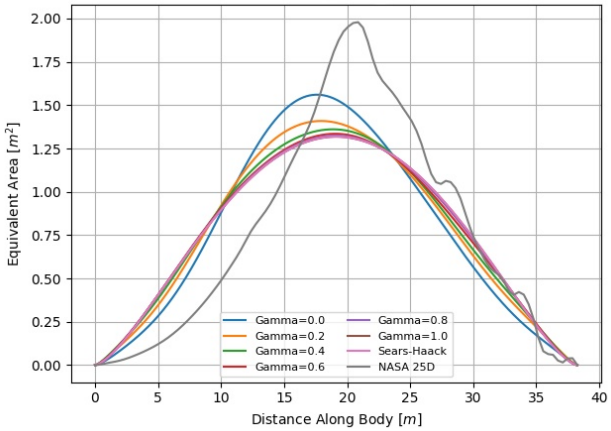

Fig. 4.7: Equivalent area distributions as the objective function shifts from minimizing boom to minimizing drag when using eight design coefficients.

The results using ten coefficients further support the trends outlined above. The minimum noise solution for an axisymmetric body is a solution that shifts the equivalent area distribution away from the forward and aft positions and towards the center of the body. This creates a higher maximum equivalent area than the solutions that minimize drag. The results are shown in Figure 4.8

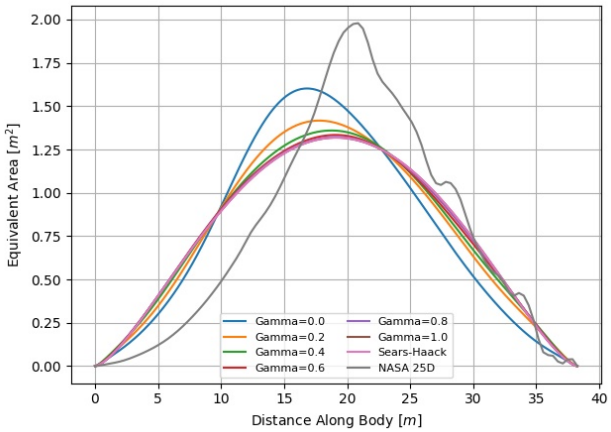

Fig. 4.8: Equivalent area distributions as the objective function shifts from minimizing boom to minimizing drag when using ten design coefficients.

Figure 4.9 presents the equivalent area distributions that produced the minimum noise solution for each number of Fourier coefficients tested.

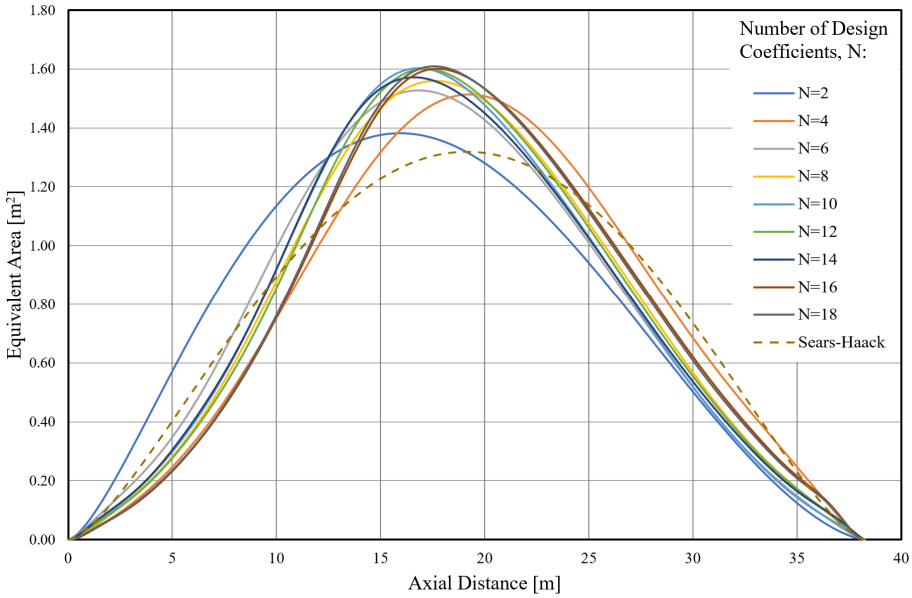

Fig. 4.9: Equivalent area distributions that produced minimum noise for a given number of design coefficients N.

The equivalent area distributions using fewer design variables oscillate forward and aft with each two design coefficients added. This is most noticeable between the minimum noise solutions when N=2 and when N=4. However, this oscillation becomes less drastic as more design coefficients are used. This supports the idea that adding coefficients will eventually reach a point of diminishing returns once the solution has converged.

Figure 4.9 also suggests that the converged solution producing minimum noise experiences a peak equivalent area value at a location that is slightly forward of the midpoint along the longitudinal axis, whereas the Sears-Haack is symmetric at the midpoint. Future work could investigate how the rate of change in area growth from Whitham's F-Function contributes to the pressure signatures generated by the minimum noise geometry.

4.6.1 Using Fourier Coefficients to Approximate a Solution to the NASA 25D

With the equivalent area distribution for a minimum noise solution known, the researchers sought to compare the NASA 25D area distribution to the minimum noise solutions using the tool set outlined in this work. A digital spreadsheet was used to find the Fourier coefficients that approximated the NASA 25D area distribution with respect to volume.

The approximated solution was produced using a solver that iterated on 18 design coefficients to minimize the error between the approximate solution and the equivalent area of the NASA 25D with respect to volume. Those design coefficients were used in the methods explained in Chapter 2 to produce the PLdB, wave drag, and the equivalent area distribution for an approximate solution of the NASA 25D's equivalent area distribution with respect to volume. This allowed for a PLdB and wave drag result to be produced for the NASA 25D using only the methods produced in this work.

4.6.2 Comparison of Equivalent Areas

With the approximate solution to the NASA 25D known, the most prominent equivalent area distributions could be compared. These equivalent area distributions are: the equivalent area for minimum noise using 18 design variables, the equivalent area of the Sears-Haack body, the NASA 25D equivalent area with respect to volume, and the approximate equivalent area distribution for the NASA 25D using 18 Fourier coefficients. These four area distributions are shown in Figure 4.10.

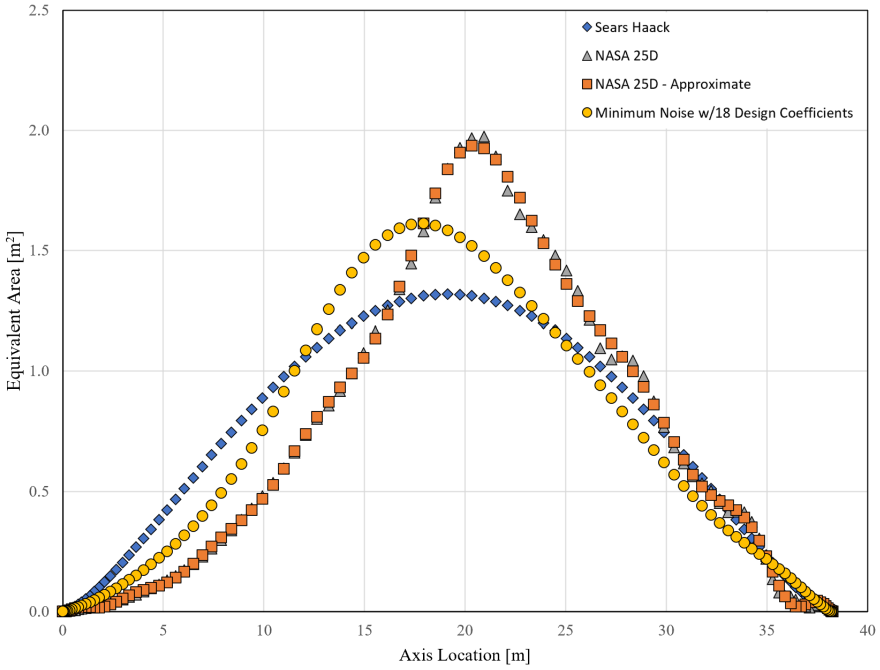

Fig. 4.10: Equivalent area distributions with respect to volume for the Sears-Haack, the minimum noise, the NASA 25D and the approximate 25D solution.

These equivalent area distributions show how the geometry of the NASA 25D aircraft relates to the geometry of the two optimized axisymmetric bodies of equal length.

4.7 Comments on Results to NASA 25D Aircraft

It is worth noting that an axisymmetric body without wings was used to produce the equivalent area distributions in this work. It is possible that the placement of wings or other lifting surfaces on the NASA 25D aircraft causes the optimal equivalent area distribution for the NASA 25D to shift further aft along its axial distance to reduce noise. As mentioned previously, lift was not accounted for in the equivalent area representations for this work, but the geometries of the lifting surfaces could still affect the equivalent area distribution when compared to the geometry of the axisymmetric body.

Figure 4.11 compares the Pareto fronts created in this work with two NASA 25D solutions. The PLdB portion of the NASA 25D(A) solution was generated from the full

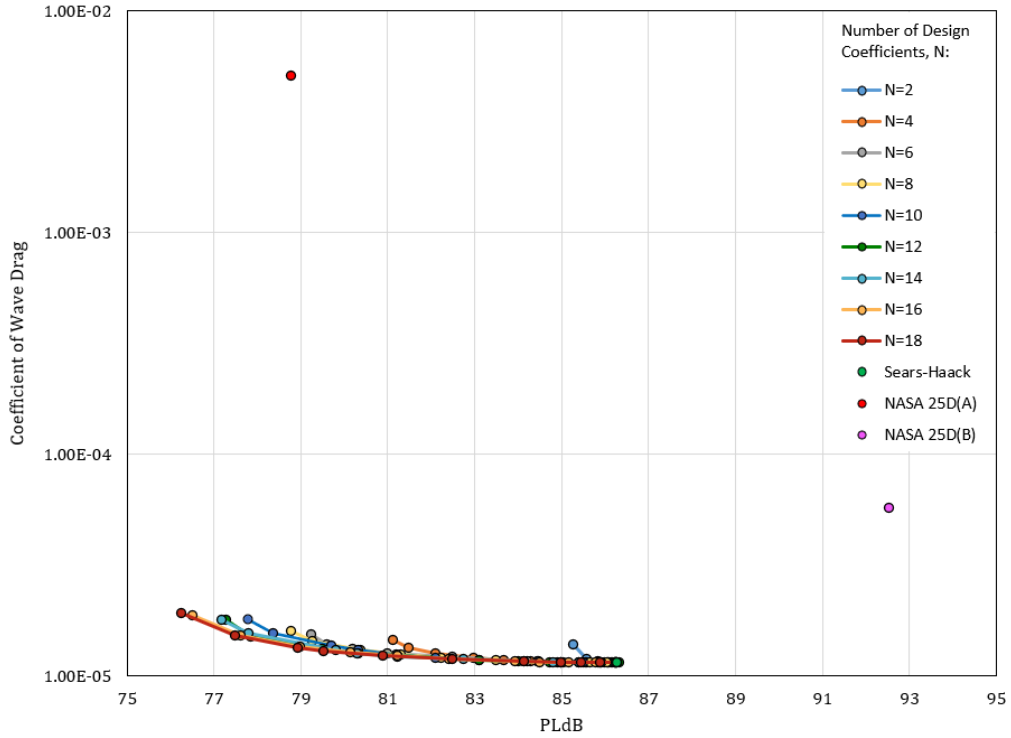

Fig. 4.11: Comparison of Pareto fronts with the approximated 18 coefficient NASA 25D results and the NASA 25D solution from using CFD/OpenVSP. Note the log scale on the y-axis.

CFD result and is in the same range of PLdB values as the Pareto fronts generated in this work. The wave drag component of that solution is based solely on the volume and was generated using OpenVSP. The NASA 25D(B) solution shown in Figure 4.11 uses the equivalent area distribution of the approximated NASA 25D solution using 18 coefficients in the Fourier sine series. The approximated solution of the NASA 25D with respect to volume is significantly louder than the others but contains a wave drag solution that is the same order of magnitude as those in the Pareto fronts. This NASA 25D(B) solution was generated using the tool set outlined in Chapter 2.

By comparing these solutions on Figure 4.11 we can find a correlation between 3rd party results as to what the PLdB and wave drag with respect to volume are for the NASA 25D aircraft. This could also show a connection where the lift components create more wave drag, but lift adjusts the equivalent area distribution in a way that reduces PLdB.

Figure 4.12 compares the Pareto front when N=18 to the approximated NASA 25D solution using 18 design coefficients. Both results were using equivalent areas with respect to volume only. The Pareto front shows a quieter solution on all accounts, and the NASA 25D produces a louder result when only using the volume component of the equivalent area distribution. The 25D was not designed using the volume of equivalent area alone. Therefore, it isn't surprising that a minimized solution would perform better than a representation from an actual aircraft. Figure 4.12 gives a point of comparison between the minimized solution with 18 coefficients and the approximated 25D solution. This 25D result shown in Figure 4.12 is the same result as the approximated NASA 25D solution generated in Figure 4.10 and Figure 4.11, respectively.

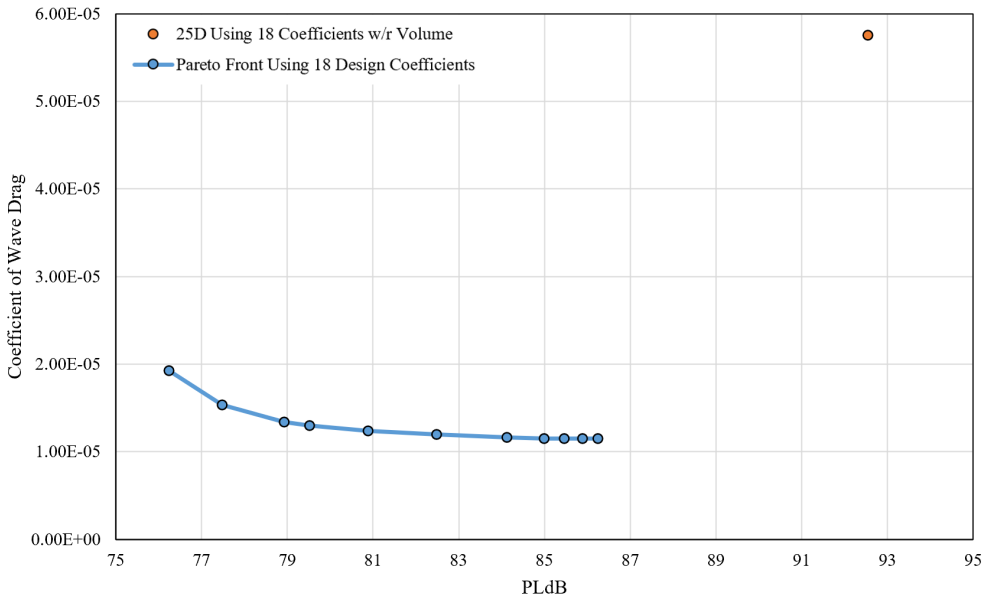

Fig. 4.12: Comparison of the Pareto front with 18 coefficients to the approximated NASA 25D equivalent area described using 18 coefficients.

Table 4.1 presents the minimum noise solution generated by each each test case using N coefficients. Additionally, the talbe presents the associated coefficient of wave drag and the Fourier coefficients used to describe equivalent area distribution for each solution.

Table 4.1: Minimum noise solutions for each set of design coefficients with the associated wave drag and Fourier coefficients along with the NASA 25D approximation.

	N=2	N=4	N=6	N=8	N=10	N=18	25D
PLdB	85.26975	81.12707	79.2448	78.76122	77.80097	76.23544	92.53553
C_{Dw}	1.39E-05	1.46E-05	1.55E-05	1.60E-05	1.79E-05	1.93E-05	5.75E-05
A1	0	0	0	0	0	0	0
A2	-0.00270	-0.00270	-0.00270	-0.00270	-0.00270	-0.00270	-0.00270
A3	0.00101	-0.00032	0.00053	0.00019	0.00040	-0.00009	-0.00100
A4	-0.00001	0.00066	0.00067	0.00085	0.00092	0.00092	0.00132
A5	0	-0.00025	-0.00039	-0.00042	-0.00048	-0.00048	0.00050
A6	0	-0.00052	-0.00035	-0.00047	-0.00048	-0.00071	-0.00079
A7	0	0	0.00027	0.00020	0.00037	0.00022	-0.00023
A8	0	0	-0.00023	-0.00013	-0.00021	-0.00004	-0.00064
A9	0	0	0	-0.00013	-0.00018	-0.00029	0.00049
A10	0	0	0	0.00000	0.00000	0.00000	-0.00054
A11	0	0	0	0	4.08E-05	1.57E-04	-4.98E-04
A12	0	0	0	0	-1.24E-04	7.73E-06	2.08E-05
A13	0	0	0	0	0	4.78E-07	-5.94E-05
A14	0	0	0	0	0	1.93E-04	-9.95E-04
A15	0	0	0	0	0	7.72E-05	-8.06E-04
A16	0	0	0	0	0	7.39E-05	-3.07E-05
A17	0	0	0	0	0	5.07E-05	4.02E-04
A18	0	0	0	0	0	1.01E-04	1.50E-04
A19	0	0	0	0	0	-6.93E-06	1.25E-04
A20	0	0	0	0	0	1.80E-05	5.06E-04

Table 4.2 presents the PLdB values in connection with the Pareto fronts presented in Figure 4.1.

Table 4.2: PLdB values along the Pareto fronts for each set of design coefficients.

Γ	N=2	N=4	N=6	N=8	N=10	N=18
0.0	85.26975	81.12707	79.2448	78.76122	77.80097	76.23544
0.1	85.56872	81.47224	79.58660	79.25697	78.35730	77.47878
0.2	85.83024	82.09040	80.20049	80.36430	80.31199	78.92561
0.3	85.98799	82.96196	80.99748	81.30470	81.20332	79.51885
0.4	86.07631	83.66378	82.48076	82.23322	82.08244	80.88805
0.5	86.13635	84.27799	84.20581	83.49351	83.10814	82.48892
0.6	86.17203	84.99095	84.98744	84.43014	84.46665	84.12815
0.7	86.20505	85.55568	85.56041	85.03242	84.89064	84.98657
0.8	86.22890	85.87775	85.86128	85.65644	85.49623	85.45196
0.9	86.24652	86.06741	86.06405	86.02794	85.89999	85.88051
1.0	86.24652	86.24652	86.25569	86.24962	86.24146	86.24002

Finally, Table 4.3 presents the coefficients of wave drag in connection with the Pareto fronts presented in Figure 4.1.

Table 4.3: Coefficients of Wave Drag along the Pareto fronts for each set of design coefficients.

Γ	N=2	N=4	N=6	N=8	N=10	N=18
0.0	1.390E-05	1.461E-05	1.546E-05	1.602E-05	1.788E-05	1.928E-05
0.1	1.196E-05	1.339E-05	1.389E-05	1.437E-05	1.568E-05	1.531E-05
0.2	1.164E-05	1.266E-05	1.319E-05	1.303E-05	1.306E-05	1.342E-05
0.3	1.154E-05	1.212E-05	1.269E-05	1.245E-05	1.245E-05	1.296E-05
0.4	1.150E-05	1.186E-05	1.216E-05	1.208E-05	1.210E-05	1.239E-05
0.5	1.149E-05	1.170E-05	1.171E-05	1.177E-05	1.185E-05	1.195E-05
0.6	1.148E-05	1.157E-05	1.157E-05	1.161E-05	1.160E-05	1.163E-05
0.7	1.148E-05	1.151E-05	1.151E-05	1.154E-05	1.154E-05	1.153E-05
0.8	1.148E-05	1.149E-05	1.149E-05	1.149E-05	1.150E-05	1.150E-05
0.9	1.148E-05	1.148E-05	1.148E-05	1.148E-05	1.148E-05	1.148E-05
1.0	1.148E-05	1.148E-05	1.148E-05	1.148E-05	1.148E-05	1.148E-05

CHAPTER 5

SUMMARY OF RESULTS AND CONCLUSIONS

The Sears-Haack solution is an axisymmetric geometry that minimizes wave drag for a given length and volume. The objective of the current work was to find an axisymmetric geometry that minimized the noise perceived from a sonic boom given a length and volume. Additionally, this research intended to further define the relationship between wave drag and the perceived loudness of a sonic boom.

Modern aircraft have the ability to alter their outer-mold line during flight. This change in the outer-mold line affects both the aerodynamic and geometric characteristics of the aircraft. Wave drag and the sonic boom are both affected by the rate of area growth along the axial distance of an aerodynamic body, but there is a trade-off to be considered as the equivalent area distribution changes.

It has been shown in this work and others that the equivalent area distribution for the Sears-Haack solution minimizes the rate of area growth for a given length and volume, thus minimizing wave drag. Based on the equivalent area distributions produced in this work, a similar observation can be made for the solution that minimized noise. The minimum noise solution is one that redistributes the equivalent area from the nose of the aircraft towards the center of the axial length along the body creating a higher peak equivalent area than that of the Sears-Haack. This characteristic of a low-boom supersonic body can be seen in equivalent area distribution of the NASA 25D aircraft.

This difference in how the equivalent area is distributed indicates there is a theoretical trade-off between wave drag and sonic boom loudness as equivalent area changes on a supersonic body. The Pareto-fronts generated in this work define the set of minimum solutions for a number of design coefficients that minimize both objectives. The information gained from these solution sets further define the relationship between wave drag and the perceived loudness of a sonic boom.

In this work and for an axisymmetric geometry, the PLdB was shown to be reduced by 10.03 decibels by accepting a 67.96% increase relative to the minimum wave drag when using 18 design coefficients for the Sears-Haack body. From a more practical standpoint, the PLdB was shown to decrease by 6.721 decibels with a 12.88% increase to the coefficient of wave drag when Γ was set to 0.3. This is a much easier trade-off to accept when considering the force of wave drag on a supersonic body. This relationship between wave drag and PLdB further supports the idea that a morphing aircraft can alter its PLdB value without changing its flight conditions if the operators are willing to accept a change in wave drag as a result. Future supersonic aircraft could incorporate the information gained from similar Pareto fronts into future designs and decision-making. A morphing supersonic airliner could temporarily reduce the audible intensity of the sonic boom over a populated area while accepting a penalty to wave drag if it was able to alter its equivalent area distribution in an optimal way.

Future work on this research would include adding the lift component to the equivalent area representation. The lift component adds complexity to the Fourier sine series representation because the sine series would need contain more frequencies and thus require more coefficients to define the equivalent area distribution. The equivalent area distributions with lift end in a non-zero value, so the von-Karman axisymmetric body would be an appropriate representation for the initial test cases, since the von-Karman body is the geometry that minimizes wave drag for a given volume and finite base area.

The current tool set could be used to study the convergence of solutions with each additional design coefficient. This work has shown a relationship between wave drag and PLdB, and it has found an axisymmetric geometry that minimizes noise for a set number of design coefficients. The convergence of these solutions could be studied in greater depth to define the sensitivity of wave drag and PLdB to additional design coefficients.

Lastly, additional work could be done to enhance the optimization routine. The optimization routine could be changed to integrate a non-dominated sorting genetic algorithm (NSGA). The NSGA algorithm is a genetic algorithm specifically tailored to optimizing a

Pareto front for a multi-objective optimization problem. This would assist in solving the optimization problem more efficiently and lower the searching time while ensuring the global minimum solution is obtained.

REFERENCES

[1] Abraham, T., *Sonic Boom Loudness Reduction Through Localized Supersonic Aircraft Equivalent-Area Changes*, Master's thesis, Utah State University, Logan, UT, 2021.

[2] John D. Anderson, J., *Fundamentals of Aerodynamics, 6th Edition*, McGraw-Hill Education, New York, N.Y., 2017.

[3] Federal Aviation Regulations, "14 C.F.R. §91.817, Civil aircraft sonic boom," 2019.

[4] Candel, S., "Concorde and the Future of Supersonic Transport," *Journal of Propulsion and Power*, Vol. 20, No. 1, 2004.

[5] Boom, "Boom Supersonic Selects Greensboro, North Carolina for First Supersonic Airliner Manufacturing," 2022-01-26 (Accessed 2022-02-23), `https://boom-press-assets.s3.us-west-2.amazonaws.com/Boom_Supersonic_Overture_Superfactory_Announcement.pdf`.

[6] Hershey, H., "Sonic Boom Structural Damage," Technical Report ADA028512, Federal Aviation Administration, 1976.

[7] Carpenter F. L., Cizmas P. G., R. S. R., "Controlling Sonic Loudness Through Outer Mold Line Modification: A Sensitivity Study," *AIAA Scitech 2019, San Diego*, 2019.

[8] Rallabhandi, S., *Sonic Boom Minimization through Vehicle Shape Optimization and Probalistic Acoustic Propagation*, Ph.D. thesis, Georgia Institute of Technology, Atlanta, 2005.

[9] Raymer, D. P., "Aerodynamic Forces," *Aircraft Design: A Conceptual Approach*, chap. 12, American Institute of Aeronautics and Astronautics, Inc., 2nd ed., 1992, pp. 258–262.

[10] Whitcomb, R. T., "A Study of the Zero-Lift Drag-Rise Characteristics of Wing-Body Combinations Near the Speed of Sound," Technical Report 1273, National Advisory Committee for Aeronautics, 1956.

[11] Kulfan, B., "Fundamentals of Supersonic Wave Drag," *Fourth International Conference on Flow Dynamics*, 2007.

[12] Ordaz, I., Geiselhart, K. A., and Fenbert, J. W., "Conceptual Design of Low-Boom Aircraft with Flight Trim Requirement," *Journal of Aircraft*, Vol. 52, No. 3, 2015, pp. 932–939.

[13] Ordaz, I., Wintzer, M., and Rallabhandi, S. K., "Full-Carpet Design of a Low-Boom Demonstrator Concept," AIAA Paper 2015–2261, 2015.

[14] Ueno, A., Kanamori, M., and Makino, Y., "Multi-fidelity Low-boom Design Based on Near-field Pressure Signature," *54th AIAA Aerospace Sciences Meeting*, 2016, p. 2033, 00007.

[15] Giblette, T. and Hunsaker, D. F., "Prediction of Sonic Boom Loudness Using High-Order Panel Methods for the Near-Field Solution," *AIAA Scitech 2019, San Diego*, 2019.

[16] Giblette, T., *Rapid Prediction of Low-Boom and Aerodynamic Performance of Supersonic Transport Aircraft Using Panel Methods*, Master's thesis, Utah State University, Logan, UT, 2019.

[17] Carpenter, F. L., Cizmas, P., Bolander, C. R., Giblette, T. N., and Hunsaker, D. F., "A Multi-Fidelity Optimization Study Investigating Distributed Adaptivity for Robust Low-Boom Performance," *AIAA Aviation 2019 Forum*, 2019, p. 3237.

[18] Bolander, C. R. and Hunsaker, D. F., "Near-field Pressure Signature Splicing for Low-Fidelity Design Space Exploration of Supersonic Aircraft," *AIAA Scitech 2020, Orlando*, 2020.

[19] Weaver-Rosen, J. M., Carpenter, F. L., Cizmas, P. G. A., Malak, R. J., Abraham, T. A., Hunsaker, D. F., and Lazzara, D. S., "Computational Design Methodology of Adaptive Outer Mold Line for Low En-Route Noise of a Supersonic Aircraft," *AIAA Scitech 2021*, 2021.

[20] Abraham, T. A., Hunsaker, D. F., Weaver-Rosen, J. M., and Malak, R. J., "Identifying Optimal Equivalent Area Changes to Reduce Sonic Boom Loudness," *AIAA Scitech 2020, Orlando*, 2020.

[21] Rallabhandi, S. K., "Advanced Sonic Boom Prediction Using the Augmented Burgers Equation," *Journal of Aircraft*, Vol. 48, No. 4, 2011, pp. 1245–1253.

[22] Abraham, T. A. and Hunsaker, D. F., "Multi-Fidelity Comparison of Supersonic Wave Drag Prediction Methods Using Axisymmetric Bodies," *AIAA Scitech 2023, National Harbor*, 2023.

[23] Ashley, H. and Landahl, M., *Aerodynamics of Wings and Bodies*, Dover Publications, Inc, Mineola, N.Y., 1985.

[24] Phillips, W. F., *Mechanics of Flight, 2nd Edition*, John Wiley Sons, Inc.-Hill Education, Hoboken, N.J., 2010.

[25] Anderson, J., *Modern Compressible Flow, 3rd Edition*, McGraw-Hill Education, New York, N.Y., 2017.

[26] Yamashita, H. and Obayashi, S., "Sonic Boom Variability Due to Homogeneous Atmospheric Turbulence," *Journal of Aircraft*, Vol. 46, No. 6, 2009, pp. 1886–1893.

[27] Whitham, G. B., "The Flow Pattern of a Supersonic Projectile," *Communications of Pure and Applied Mathematics*, Vol. 5, No. 3, 1952, pp. 301–347.

[28] Seebass, R. A., "Sonic Boom Theory," *Journal of Aircraft*, Vol. 6, No. 3, 1969, pp. 177–184.

[29] Carlson, H. W. and Maglieri, D. J., "Review of Sonic-Boom Generation Theory and Prediction Methods," *The Journal of the Acoustical Society of America*, Vol. 51, No. 2C, 1972, pp. 675–685.

[30] Lomax, H., "The Wave Drag of Arbitrary Configurations in LInearized Flow as Determined by Areas and Forces in Oblique Planes," Technical Report RM A55A18, NACA, 1955.

[31] Plotkin, K. J., "Review of Sonic boom Theory," *AIAA 12th Aeroacoustics Conference*, 1989.

[32] Jones, R. T., "Theory of Wing-Body Drag at Supersonic Speeds," Technical Report 19930092281, NASA, 1956.

[33] Seebass, R. A. and Argrow, B., "Sonic Boom Minimization Revisited," *Theoretical Fluid Mechanics Meeting*, 1998.

[34] Lomax, H. and Heaslet, M. A., "Recent Developments in the Theory of Wing-Body Wave Drag," *Journal of the Aeronautical Sciences*, Vol. 23, No. 12, 1956.

[35] Stevens, S., "Perceived level of noise by Mark VII and decibels (E)," *The Journal of the Acoustical Society of America*, Vol. 51, No. 2B, 1972, pp. 575–601.

[36] Waddington, M. J., *Development of An Interactive Wave Drag Capability for the OPENVSP Parametric Geometry Tool*, Master's thesis, California Polytechnic State University, San Luis Obispo, 2015.

[37] OpenVSP, 2022, `URL:http://openvsp.org/.`